A Numerical Study of Ocean Polarimetric Thermal Emission

Joel T. Johnson, *Member, IEEE*, Robert T. Shin, *Senior Member, IEEE*, Jin Au Kong, *Fellow, IEEE*, Leung Tsang, *Fellow, IEEE*, and Kyung Pak

***Abstract*—A numerical model for polarimetric thermal emission from penetrable ocean surfaces rough in two directions is presented. The numerical model is based on Monte Carlo simulation with an iterative version of the method of moments (MOM) known as the sparse matrix flat surface iterative approach (SMFSIA), extended to the penetrable surface case through a numerical impedance boundary condition (NIBC) method. Since the small U_B brightnesses obtained from ocean surfaces (usually less than 1.5 K, or 0.5% of a 300-K physical temperature) require extremely accurate simulations to avoid large errors, a parallel version of the algorithm is developed to allow matrix elements to be integrated accurately and stored. The high accuracy required also limits simulations to near flat surface profiles, so that only high-frequency components of the ocean spectrum are modeled. Variations in nadir polarimetric brightness temperatures with spectrum low- and high-frequency cutoffs show the Bragg (or shortwave) portion of the spectrum to contribute significantly to emission azimuthal signatures, as predicted by the small perturbation or composite surface approximate theories. Quantitative comparisons with approximate methods show perturbation theory to slightly overestimate linear brightness temperatures, but accurately predict their azimuthal variations, while physical optics (PO) significantly underestimates both linear brightness temperatures and their azimuthal variations. Further simulations with the numerical model allow sensitivities to ocean spectrum models to be investigated and demonstrate the importance of an accurate azimuthal description for the ocean spectrum.**

***Index Terms*—Emission, remote sensing, rough surfaces.**

I. Introduction

MODELS for the prediction of ocean surface polarimetric thermal emission are currently of interest for the interpretation of data from recent airborne microwave radiometer flights. As discussed in [1], vertically and horizontally polarized brightness temperatures of azimuthally anisotropic media are expected to vary with azimuth angle and contain signals in the third and fourth Stokes parameters U_B and V_B. Since a wind-generated ocean surface has such azimuthally anisotropic properties, polarimetric passive remote sensing should be useful for the remote sensing of ocean winds and is currently under investigation by a number of organizations [2]–[17]. Although experimental data have been taken and reveal azimuthal variations similar to those observed for fabricated surfaces, a fully validated model for the prediction of ocean polarimetric brightnesses does not presently exist.

In this paper, an initial numerical study of ocean polarimetric brightness temperatures is performed for two-dimensional (2-D) ocean surface models with the sparse matrix flat surface iterative approach (SMFSIA) of [18]–[22], which has been successfully applied to scattering of scalar and electromagnetic waves from 2-D perfectly conducting and low dielectric constant rough surfaces. Monte Carlo simulations are applied for the Durden–Vesecky ocean spectrum discussed in [23] since this spectrum has been used in previous studies [10], [11]. The influence of differing ocean length scales is studied, and predictions are compared with those of the standard approximate theories, although the large computational requirements associated with 2-D penetrable surface simulations limit maximum SMFSIA surface sizes to 8×8 electromagnetic wavelengths and the small azimuthal variations that occur (usually less than 1.5 K) make accurate calculations difficult. These limitations allow only the high-frequency portion of the ocean spectrum to be studied, resulting in small rms height surfaces in the simulations. Results show the importance of the Bragg scattering contribution to observed brightness temperatures and the insensitivity of predicted brightness temperature to longer scale ocean waves. Perturbation theory is found to accurately predict brightness temperature azimuthal variations but slightly overpredicts the constant level of linear brightness temperatures. A physical optics approach significantly underestimates both quantities. Numerical predictions are also found to be sensitive to the ocean spectral model used in the simulations, demonstrating the importance of an accurate knowledge of the azimuthal properties of the ocean surface in future models.

The next section provides a brief review of previous studies of ocean thermal emission and discusses the application of standard approximate theories to this problem. The formulation of the penetrable surface SMFSIA is presented in detail in Sections III–VII, and a validation of the technique is presented in Section VIII. Section IX presents numerical results.

Manuscript received July 1, 1996; revised August 29, 1997. This work was sponsored by ONR Contracts N00014-92-J-1616 and N00014-9710541, NASA Contract 958461, and a National Science Foundation Graduate Fellowship. Use of the IBM SP/2 at the Maui High Performance Computing Center was supported by the Phillips Laboratory, Air Force Material Command, under Cooperative Agreement F29601-93-2-0001.

J. T. Johnson is with the Department of Electrical Engineering, The Ohio State University, Columbus, OH 43210 USA (e-mail: johnson@ee.eng.ohio-state.edu).

R. T. Shin and J. A. Kong are with the Department of Electrical Engineering and Research Laboratory of Electronics, Massachusetts Institute of Technology, Cambridge, MA 02139 USA.

L. Tsang is with the Electromagnetics and Remote Sensing Laboratory, Department of Electrical Engineering, University of Washington, Seattle, WA 98195 USA.

K. Pak is with the Jet Propulsion Laboratory, MS 300-235, California Institute of Technology, Pasadena, CA 91109 USA.

Publisher Item Identifier S 0196-2892(99)00036-4.

II. Previous Studies of Ocean Polarimetric Thermal Emission

Interest in improvements in the ocean wind vector retrievals of [24] has led to the development of polarimetric techniques for ocean passive remote sensing. The brightness temperature modified Stokes vector measured in polarimetric passive remote sensing is defined as

$$\overline{T}_B = \frac{1}{C}\overline{I} = \frac{1}{C}\begin{bmatrix} I_h \\ I_v \\ U \\ V \end{bmatrix} = \frac{1}{\eta C}\begin{bmatrix} \langle E_h E_h^* \rangle \\ \langle E_v E_v^* \rangle \\ 2\,\mathrm{Re}\langle E_v E_h^* \rangle \\ 2\,\mathrm{Im}\langle E_v E_h^* \rangle \end{bmatrix}. \quad (1)$$

In the above equation, E_h and E_v are the emitted electric fields received from the horizontal and vertical polarization channels of the observing radiometer, η is the characteristic impedance, $C = K/\lambda^2$ with K denoting Boltzmann's constant, and λ is the wavelength. The first two parameters of the brightness temperature Stokes vector correspond to received powers for horizontal and vertical polarizations, respectively. The third and fourth parameters correspond to the complex correlation between electric fields received by the horizontal and vertical channels, and they can be calculated as linear combinations of brightness temperatures in three polarizations, as discussed in [1]. These four parameters are labeled T_{Bh}, T_{Bv}, U_B, and V_B, respectively, in this paper.

The emissivity of an object is defined as the ratio of the brightness temperature emitted by an object to its actual physical temperature, under the assumption that the object is at a constant physical temperature T_{phys}

$$T_{Ba} = e_a(\theta, \phi) T_{\mathrm{phys}}. \quad (2)$$

In the above equation, the subscript a refers to the polarization of the brightness temperature, θ refers to the polar observation angle, and ϕ refers to the azimuthal observation angle. Through the principles of energy conservation and reciprocity, Kirchhoff's Law relates this emissivity to the reflectivity of the surface [25]

$$e_a(\theta, \phi) = 1 - r_a(\theta, \phi) \quad (3)$$

where the reflectivity, $r_a(\theta, \phi)$ is defined to be the fraction of power scattered from a surface for an $a = h, v$ polarized wave incident from direction (θ, ϕ). From the above equation, it is clear that polarimetric brightness temperatures can be calculated using either the power absorbed (equal to e_a) or the scattered power $(1 - r_a)$ in the reciprocal scattering problem.

The small perturbation method (SPM) emission model of [10] was found to produce reasonable comparisons with the experimental data of [7] using the Durden–Vesecky spectrum once second-order contributions to the coherent reflection coefficient were taken into account. To address the effect of longer scale ocean waves, a composite surface model based on the original formulation of [26] was developed and predictions were compared with WINDRAD experimental data [11] in T_{Bh}, T_{Bv} and U_B brightnesses. Again, overall agreement in the azimuthal variations of polarimetric brightness temperatures was found to be good, although experimental data in the linearly polarized brightnesses exceeded model predictions by as much as 25 K and an empirical weighting function was included in the model to obtain the observed up–down wind brightness asymmetry. Only minor differences between brightnesses predicted by the composite surface and SPM alone models were observed, indicating that the longwave "tilting" effects of the composite surface model have little influence on azimuthal variations of ocean brightness temperatures. Differences between experimental and theoretical linear brightnesses were explained due to effects of foam and atmospheric emissions, which were not included in the theoretical model. Simulations were also performed using a geometrical optics model with the Cox and Munk derived slope variances for an ocean surface, and predicted azimuthal variations were found smaller than those of the composite surface model. Thus, [11] concludes that the most significant source of azimuthal variations in ocean surface emission is the SPM Bragg scattering contribution.

In contrast, [14]–[16] propose a Monte Carlo physical optics (PO)-based model that includes shadowing and multiple scattering effects and additional ocean surface features, such as asymmetric waves and foam, and obtain reasonable agreement with measured data from ground-based observations of mechanically generated water waves at 91.65 GHz and with satellite data at 19 and 37 GHz. A PO model for ocean emission would emphasize the longwave portion of the spectrum since near-forward scattering, in which PO predictions are expected to be valid, is dominated by surface low frequencies. It should be noted that no models have been based on an analytical PO method, due to the difficulties associated with PO integral evaluation since Fresnel reflection coefficients vary as a function of incidence angle. Monte Carlo simulations using the PO approximation to determine induced surface currents, however, are not limited by this problem since local incidence angles can be determined for a given surface realization and will be applied in this paper for comparison with SMFSIA results. The distinction between conclusions regarding the influence of ocean spectral regions on azimuthal brightness variations under a PO-based model and the composite surface model emphasizes the limited state of current knowledge in polarimetric passive remote sensing and motivates the numerical simulations of this paper. Sensitivities of ocean brightnesses with respect to surface high- and low-frequency content will be investigated to address this issue, and comparisons will be made with both SPM and Monte Carlo PO predictions to obtain some insight into the differences between these references.

III. Integral Equation Formulation

Calculation of scattering from a penetrable rough surface will be performed through a method of moments (MOM) technique [27], based on the standard magnetic field integral equation (MFIE) and electric field integral equation (EFIE) integral equations [28]

$$\frac{\overline{n} \times \overline{H}_0(\overline{r})}{2} = \overline{n} \times \overline{H}_{\mathrm{inc}} + \overline{n} \times \int dS' \cdot \Big\{ -i\omega\epsilon_0 \overline{\overline{G}}_0(\overline{r}, \overline{r}')[\hat{n}' \times \overline{E}(\overline{r}')] + \nabla \times \overline{\overline{G}}_0 \cdot [\hat{n}' \times \overline{H}(\overline{r}')] \Big\} \quad (4)$$

in region 0 above the surface profile and

$$-\frac{\overline{n}\times\overline{E}_1(\overline{r})}{2}=\overline{n}\times\int dS'\Big\{i\omega\mu_1\overline{\overline{G}}_1(\overline{r},\overline{r}')\cdot[\hat{n}'\times\overline{H}(\overline{r}')]+\nabla\times\overline{\overline{G}}_1\cdot[\hat{n}'\times\overline{E}(\overline{r}')]\Big\} \quad (5)$$

in region 1 below, where

$$\hat{n}=\frac{\left(\hat{z}-\dfrac{\partial f}{\partial x}\,\hat{x}-\dfrac{\partial f}{\partial y}\,\hat{y}\right)}{\sqrt{1+\left(\dfrac{\partial f}{\partial x}\right)^2+\left(\dfrac{\partial f}{\partial y}\right)^2}}=\frac{\overline{n}}{\sqrt{1+\left(\dfrac{\partial f}{\partial x}\right)^2+\left(\dfrac{\partial f}{\partial y}\right)^2}}$$

is a unit normal vector to the surface $z=f(x,y)$. The region above the surface profile is assumed to be free space, and the region below to be a homogeneous, isotropic medium described by electric permittivity ϵ_1 and magnetic permeability μ_0, and a time dependency of $e^{-i\omega t}$ is implied. The dyadic Green's function of the above equations is given by

$$\overline{\overline{G}}_j=\left[\overline{\overline{I}}+\frac{1}{k_j^2}\nabla\nabla\right]g_j(\overline{r},\overline{r}') \quad (6)$$

where $\overline{\overline{I}}$ represents the unit dyadic, k_j is the electromagnetic wavenumber $\omega\sqrt{\mu_0\epsilon_j}$, and

$$g_j(\overline{r},\overline{r}')=\frac{e^{ik_j|\overline{r}-\overline{r}'|}}{4\pi|\overline{r}-\overline{r}'|} \quad (7)$$

is the scalar Green's function. Note that integrals in (4) and (5) are principle value integrals with the factor of 1/2 on the left-hand side resulting from the dyadic Green's function singularity.

Difficulties associated with principle value integration of the self terms in the above formulation motivate a transformation to the Stratton–Chu integral equations, as discussed in [29]. The equations then become

$$\begin{aligned}&\frac{\overline{n}\times\overline{H}(\overline{r})}{2}\\&=\overline{n}\times\overline{H}_{\rm inc}+\overline{n}\times\int dS'\\&\cdot\Big\{-i\omega\epsilon_0 g_0(\overline{r},\overline{r}')[\hat{n}'\times\overline{E}(\overline{r}')]+\nabla g_0\times[\hat{n}'\times\overline{H}(\overline{r}')]\\&\quad-\frac{i}{\omega\mu_0}\nabla_s'\cdot[\hat{n}'\times\overline{E}(\overline{r}')]\nabla g_0\Big\}\end{aligned} \quad (8)$$

in region 0 above the surface profile and

$$\begin{aligned}&-\frac{\overline{n}\times\overline{E}(\overline{r})}{2}\\&=\overline{n}\times\int dS'\\&\cdot\Big\{i\omega\mu_1 g_1(\overline{r},\overline{r}')\cdot[\hat{n}'\times\overline{H}(\overline{r}')]+\nabla g_1\times[\hat{n}'\times\overline{E}(\overline{r}')]\\&\quad+\frac{i}{\omega\epsilon_1}\nabla_s'\cdot[\hat{n}'\times\overline{H}(\overline{r}')]\nabla g_1\Big\}.\end{aligned} \quad (9)$$

Applying the MOM to these equations requires expansion of the four unknown scalar functions on the surface into pulse basis functions $P_{mn}(\overline{r})$ as

$$F_x=\hat{x}\cdot\big[\hat{n}\times\overline{H}(\overline{r})\big]=\sum_m\sum_n F_x^{mn}P_{mn}(\overline{r}) \quad (10)$$

$$F_y=\hat{y}\cdot\big[\hat{n}\times\overline{H}(\overline{r})\big]=\sum_m\sum_n F_y^{mn}P_{mn}(\overline{r}) \quad (11)$$

$$G_x=\hat{x}\cdot\big[\hat{n}\times\overline{E}(\overline{r})\big]=\sum_m\sum_n G_x^{mn}P_{mn}(\overline{r}) \quad (12)$$

$$G_y=\hat{y}\cdot\big[\hat{n}\times\overline{E}(\overline{r})\big]=\sum_m\sum_n G_y^{mn}P_{mn}(\overline{r}) \quad (13)$$

and substituting these expansions into dot products of (8) and (9) with $\hat{x}$ and $\hat{y}$, respectively. The resulting four scalar equations are

$$\begin{aligned}&H_y^{\rm inc}+\frac{\partial f}{\partial y}H_z^{\rm inc}\\&=-\frac{F_x\sqrt{1+\left(\dfrac{\partial f}{\partial x}\right)^2+\left(\dfrac{\partial f}{\partial y}\right)^2}}{2}\\&\quad+\int_{-L_y/2}^{L_y/2}\int_{-L_x/2}^{L_x/2}dx'\,dy'\sqrt{1+\left(\frac{\partial f}{\partial x'}\right)^2+\left(\frac{\partial f}{\partial y'}\right)^2}\\&\quad\times\Big\{-i\omega\epsilon_0 g_0\Big[-G_x\frac{\partial f}{\partial y}\frac{\partial f}{\partial x'}-G_y\Big(1+\frac{\partial f}{\partial y}\frac{\partial f}{\partial y'}\Big)\Big]\\&\qquad+G_{30}\Big[F_x\Big(dy\frac{\partial f}{\partial y}+dx\frac{\partial f}{\partial x'}-dz\Big)\\&\qquad\quad+F_y\Big(\frac{\partial f}{\partial y'}-\frac{\partial f}{\partial y}\Big)dx\Big]\\&\qquad+\frac{i}{\omega\mu_0}\nabla_s'\cdot\overline{G}\Big[dy+\frac{\partial f}{\partial y}dz\Big]G_{30}\Big\}\end{aligned} \quad (14)$$

$$\begin{aligned}&-H_x^{\rm inc}-\frac{\partial f}{\partial x}H_z^{\rm inc}\\&=-\frac{F_y\sqrt{1+\left(\dfrac{\partial f}{\partial x}\right)^2+\left(\dfrac{\partial f}{\partial y}\right)^2}}{2}\\&\quad+\int_{-L_y/2}^{L_y/2}\int_{-L_x/2}^{L_x/2}dx'\,dy'\sqrt{1+\left(\frac{\partial f}{\partial x'}\right)^2+\left(\frac{\partial f}{\partial y'}\right)^2}\\&\quad\times\Big\{-i\omega\epsilon_0 g_0\Big[G_x\Big(1+\frac{\partial f}{\partial x}\frac{\partial f}{\partial x'}\Big)+G_y\frac{\partial f}{\partial y'}\frac{\partial f}{\partial x}\Big]\\&\qquad+G_{30}\Big[F_x\Big(\frac{\partial f}{\partial x'}-\frac{\partial f}{\partial x}\Big)dy\\&\qquad\quad+F_y\Big(dy\frac{\partial f}{\partial y'}+dx\frac{\partial f}{\partial x}-dz\Big)\Big]\\&\qquad-\frac{i}{\omega\mu_0}\nabla_s'\cdot\overline{G}\Big[dx+\frac{\partial f}{\partial x}dz\Big]G_{30}\Big\}\end{aligned} \quad (15)$$

$$
\begin{aligned}
0 = & \frac{G_x\sqrt{1+\left(\frac{\partial f}{\partial x}\right)^2+\left(\frac{\partial f}{\partial y}\right)^2}}{2} \\
& + \int_{-L_y/2}^{L_y/2}\int_{-L_x/2}^{L_x/2} dx'\,dy'\sqrt{1+\left(\frac{\partial f}{\partial x'}\right)^2+\left(\frac{\partial f}{\partial y'}\right)^2} \\
& \times \left\{ i\omega\mu_0 g_1\left[-F_x\frac{\partial f}{\partial y}\frac{\partial f}{\partial x'} - F_y\left(1+\frac{\partial f}{\partial y}\frac{\partial f}{\partial y'}\right)\right]\right. \\
& \quad + G_{31}\left[G_x\left(dy\frac{\partial f}{\partial y}+dx\frac{\partial f}{\partial x'}-dz\right)\right. \\
& \qquad \left. + G_y\left(\frac{\partial f}{\partial y'}-\frac{\partial f}{\partial y}\right)dx\right] \\
& \quad \left. - \frac{i}{\omega\epsilon_1}\nabla_s'\cdot\overline{F}\left[dy+\frac{\partial f}{\partial y}dz\right]G_{31}\right\} \qquad (16)
\end{aligned}
$$

$$
\begin{aligned}
0 = & \frac{G_y\sqrt{1+\left(\frac{\partial f}{\partial x}\right)^2+\left(\frac{\partial f}{\partial y}\right)^2}}{2} \\
& + \int_{-L_y/2}^{L_y/2}\int_{-L_x/2}^{L_x/2} dx'\,dy'\sqrt{1+\left(\frac{\partial f}{\partial x'}\right)^2+\left(\frac{\partial f}{\partial y'}\right)^2} \\
& \times \left\{ i\omega\mu_0 g_1\left[F_x\left(1+\frac{\partial f}{\partial x}\frac{\partial f}{\partial x'}\right)+F_y\frac{\partial f}{\partial y'}\frac{\partial f}{\partial x}\right]\right. \\
& \quad + G_{31}\left[G_x\left(\frac{\partial f}{\partial x'}-\frac{\partial f}{\partial x}\right)dy\right. \\
& \qquad \left. + G_y\left(dy\frac{\partial f}{\partial y'}+dx\frac{\partial f}{\partial x}-dz\right)\right] \\
& \quad \left. + \frac{i}{\omega\epsilon_1}\nabla_s'\cdot\overline{F}\left[dx+\frac{\partial f}{\partial x}dz\right]G_{31}\right\} \qquad (17)
\end{aligned}
$$

which are then tested at the center points of the pulse basis functions to form the matrix equation of the MOM. In the above equations

$$
\begin{aligned}
\nabla g_j(\overline{r},\overline{r}') &= \overline{R}\,\frac{e^{ik_j|\overline{r}-\overline{r}'|}}{4\pi|\overline{r}-\overline{r}'|^2}\left(ik_j-\frac{1}{|\overline{r}-\overline{r}'|}\right) \\
&= \overline{R}G_{3j}
\end{aligned}
$$

where

$$
\begin{aligned}
\overline{R} &= \hat{x}(x-x')+\hat{y}(y-y')+\hat{z}(f(x,y)-f(x',y')) \\
&= \hat{x}\,dx+\hat{y}\,dy+\hat{z}\,dz. \qquad (18)
\end{aligned}
$$

Note that the $\nabla_s'\cdot\overline{G}$ and $\nabla_s'\cdot\overline{F}$ terms require a numerical differentiation of unknown functions and are calculated as

$$
\begin{aligned}
\nabla_s'\cdot\overline{A} &\approx \frac{\partial}{\partial x'}A_x+\frac{\partial}{\partial y'}A_y \\
&\approx \left(F_x^{n+1,m}-F_x^{n-1,m}\right)/(2\Delta x) \\
&\quad + \left(F_y^{n,m+1}-F_y^{n,m-1}\right)/(2\Delta y) \qquad (19)
\end{aligned}
$$

where n and m refer to the x and y indexes of the pulse basis functions used on the surface rectangular grid and Δx and Δy refer to the spacing between these basis functions in the x and y directions. Derivatives at points on surface edges are computed by assuming currents at the adjacent point are zero; note that this is not a large source of error since a tapered incident field will be used to eliminate fields at surface edges. Surfaces in this formulation are approximated as a collection of planes, with their heights and first derivatives specified on a rectangular grid. The above procedure for the calculation of surface field divergences effectively assumes that adjacent field values are averaged with the center point to obtain values for surface fields at the edges of the center pulse basis function, and these values then derive the divergence through a centered difference derivative. The accuracy of this approximation was investigated through comparison of results with a six unknown-function penetrable code, in which surface field divergences were retained also as unknown functions. Obtained values were found to correspond well with (19).

Note also that the g_j and $\nabla_s'\cdot\overline{A}$ functions have singularity contributions when the testing and integration points overlap, which require careful consideration. A small argument expansion of these terms was analytically integrated, and remaining portions of the these functions were integrated numerically to insure accurate calculations. Principle value integrals involving ∇g_j are zero when testing and integration points overlap for surfaces approximated by collections of planes, as can be seen in (14)–(17), due to the fact that MFIE matrix elements vanish for flat surfaces.

Other choices of integral equations could be used as well, but note that the choice illustrated results in the

$$
\frac{\sqrt{1+\left(\frac{\partial f}{\partial x}\right)^2+\left(\frac{\partial f}{\partial y}\right)^2}}{2}
$$

terms always located on matrix diagonals if sets of four (14)–(17) are taken together for individual testing points to construct the matrix equation and if unknown amplitudes are taken as sets of four in the column vector multiplied by the matrix. Since these terms are usually the largest matrix elements obtained, their inclusion on matrix diagonals improves matrix conditioning properties and iterative method convergence.

IV. Matrix Equation and Numerical Impedance Boundary Condition (NIBC)

A standard approach to the MOM would discretize (14)–(17) into a single matrix in terms of the F_x, F_y, G_x, and G_y unknown pulse basis function amplitudes. However, the high loss tangent of sea water at the microwave frequencies of interest leads to some important differences between (14)–(15) and (16)–(17). Clearly, the rapid decay of the Green's function in the lower medium allows matrix elements beyond a certain distance from the testing point to be completely neglected in (16) and (17). For example, results presented in this paper will use an ocean permittivity of $\epsilon = 39.7 + i40.2$ at 14 GHz, which corresponds to that of sea water at 10 °C with a salinity of 30 parts per thousand obtained from the model of [30]. The resulting wavenumber inside the ocean is $k_1 = 2033.6 + i849.8$, which decays to less than 1% in a distance of 5.42 mm, or 0.253 free space wavelengths. Thus, only points within a radius of 0.253 free

space wavelengths around the testing point are expected to contribute significantly. A separation of these rapidly decaying lower medium Green's functions can be obtained in the MOM matrix equation to improve matrix inversion efficiency by beginning with (16) and (17) in matrix form as

$$\begin{bmatrix} \overline{\overline{A}}_{11} & \overline{\overline{A}}_{12} & \overline{\overline{A}}_{13} & \overline{\overline{A}}_{14} \\ \overline{\overline{A}}_{21} & \overline{\overline{A}}_{22} & \overline{\overline{A}}_{23} & \overline{\overline{A}}_{24} \end{bmatrix} \begin{bmatrix} \overline{F_x} \\ \overline{F_y} \\ \overline{G_x} \\ \overline{G_y} \end{bmatrix} = \begin{bmatrix} \overline{0} \\ \overline{0} \end{bmatrix} \tag{20}$$

where the $\overline{\overline{A}}_{ij}$ matrices refer to the corresponding Green's functions integrals in (16) and (17), $\overline{F_x}$ through $\overline{G_y}$ represent vectors made of the unknown constant amplitudes of the pulse basis functions and $\overline{0}$ is a null vector. Although (20) is written as if the matrix is composed of eight $N \times N$ submatrices, submatrix elements are actually arranged so that individual 2×4 submatrices are placed adjacently for each testing-integration point combination, i.e., columns one through four of row one contain the first elements of $\overline{\overline{A}}_{11}$, $\overline{\overline{A}}_{12}$, $\overline{\overline{A}}_{13}$, and $\overline{\overline{A}}_{14}$ rather than the first four columns of $\overline{\overline{A}}_{11}$. The notation above will be used for convenience, however, in the following equations.

Equation (20) can be solved for $\overline{G}$ as

$$\begin{bmatrix} \overline{G_x} \\ \overline{G_y} \end{bmatrix} = -\overline{\overline{R}}^{-1} \overline{\overline{S}} \begin{bmatrix} \overline{F_x} \\ \overline{F_y} \end{bmatrix} \tag{21}$$

where

$$\overline{\overline{R}} = \begin{bmatrix} \overline{\overline{A}}_{13} & \overline{\overline{A}}_{14} \\ \overline{\overline{A}}_{23} & \overline{\overline{A}}_{24} \end{bmatrix} \tag{22}$$

and

$$\overline{\overline{S}} = \begin{bmatrix} \overline{\overline{A}}_{11} & \overline{\overline{A}}_{12} \\ \overline{\overline{A}}_{21} & \overline{\overline{A}}_{22} \end{bmatrix}. \tag{23}$$

Rewriting (14) and (15) in matrix form as

$$\begin{bmatrix} \overline{\overline{A}}_{31} & \overline{\overline{A}}_{32} & \overline{\overline{A}}_{33} & \overline{\overline{A}}_{34} \\ \overline{\overline{A}}_{41} & \overline{\overline{A}}_{42} & \overline{\overline{A}}_{43} & \overline{\overline{A}}_{44} \end{bmatrix} \begin{bmatrix} \overline{F}_x \\ \overline{F}_y \\ \overline{G}_x \\ \overline{G}_y \end{bmatrix} = \begin{bmatrix} -\overline{F}_x^{\text{inc}} \\ -\overline{F}_y^{\text{inc}} \end{bmatrix} \tag{24}$$

and substituting in (21) for $\overline{G}$ yields

$$\left\{ \overline{\overline{T}} - \overline{\overline{U}}\, \overline{\overline{R}}^{-1} \overline{\overline{S}} \right\} \begin{bmatrix} \overline{F}_x \\ \overline{F}_y \end{bmatrix} = \begin{bmatrix} -\overline{F}_x^{\text{inc}} \\ -\overline{F}_y^{\text{inc}} \end{bmatrix} \tag{25}$$

where

$$\overline{\overline{T}} = \begin{bmatrix} \overline{\overline{A}}_{31} & \overline{\overline{A}}_{32} \\ \overline{\overline{A}}_{41} & \overline{\overline{A}}_{42} \end{bmatrix} \tag{26}$$

and

$$\overline{\overline{U}} = \begin{bmatrix} \overline{\overline{A}}_{33} & \overline{\overline{A}}_{34} \\ \overline{\overline{A}}_{43} & \overline{\overline{A}}_{44} \end{bmatrix} \tag{27}$$

where now only the $\overline{\overline{R}}$ and $\overline{\overline{S}}$ matrices contain the lower medium Green's function, while the $\overline{\overline{T}}$ and $\overline{\overline{U}}$ terms involve the upper medium Green's function only. The first $\overline{\overline{T}}$ matrix of this equation is exactly that of the MFIE for perfectly conducting surfaces [19], so the second product of three matrices modifies the MFIE to include the effects of finite surface conductivity. While this revision of the entire matrix equation may not seem to provide a significant improvement in efficiency given the additional inversion of the $\overline{\overline{R}}$ matrix required, actually this inversion step is not costly due to the near-diagonal form of this matrix that results from rapid Green's function decay.

A strict interpretation of the MOM requires sampling at a rate ranging from four to ten points per wavelength to accurately compute lower medium Green's function integrals and model possible spatial variations of the surface fields. For materials with high dielectric constants, the short wavelengths obtained inside the dielectric material can therefore cause great increases in the number of unknowns required to solve a fixed physical size problem. However, it is clear that a limit to the discretization level needed should be obtained for highly lossy media since solutions for a perfectly conducting surface require sampling only on the scale of the free-space wavelength. Previous approaches for highly conducting surfaces have been based on the standard impedance boundary condition (IBC) [31], which approximates tangential electric fields on the surface profile as

$$\overline{E}_{\tan} = Z[\hat{n} \times \overline{H}] \tag{28}$$

where Z is the characteristic impedance of the lower medium. The IBC can be related to (21) by observing that it corresponds to ignoring any phase variations of either surface fields or Green's functions on the scale of the lower medium wavelength and approximates (16) and (17) by a single point relationship between the $\overline{G}$ and $\overline{F}$ unknown functions. The approach to be applied in this paper retains a sampling rate of eight unknowns per free-space wavelength, as in the standard IBC approach, but uses the exact (21) to determine the relationship between tangential electric and magnetic fields, and performs integrals over the lower medium Green's function numerically to capture the rapid phase variations. This method is based on the observation that fields on the surface that vary significantly faster than the free-space scale generate only evanescent waves and should not affect scattered power results. A validation will be performed in Section VIII through comparison with flat surface analytical results. At a minimum, the approach applied can be considered a numerical IBC (NIBC) extension since accurate integrals over the lower medium Green's function are performed and the single point relationship of the IBC is avoided.

V. Tapered Incident Field

One issue in Monte Carlo simulations involves the effect of finite surface size. Incident fields in the simulation are "tapered" with a Gaussian beam amplitude pattern, which confines the illuminated rough surface to the surface area $L_x \times L_y$ so that surface edges do not contribute strongly to obtained scattered fields. For nadir observation at an azimuth angle of 0°, the incident field in the simulation is a Gaussian beam designed to have no $\hat{y}$ component of the magnetic field on the planar boundary $z = 0$. Writing the general plane wave

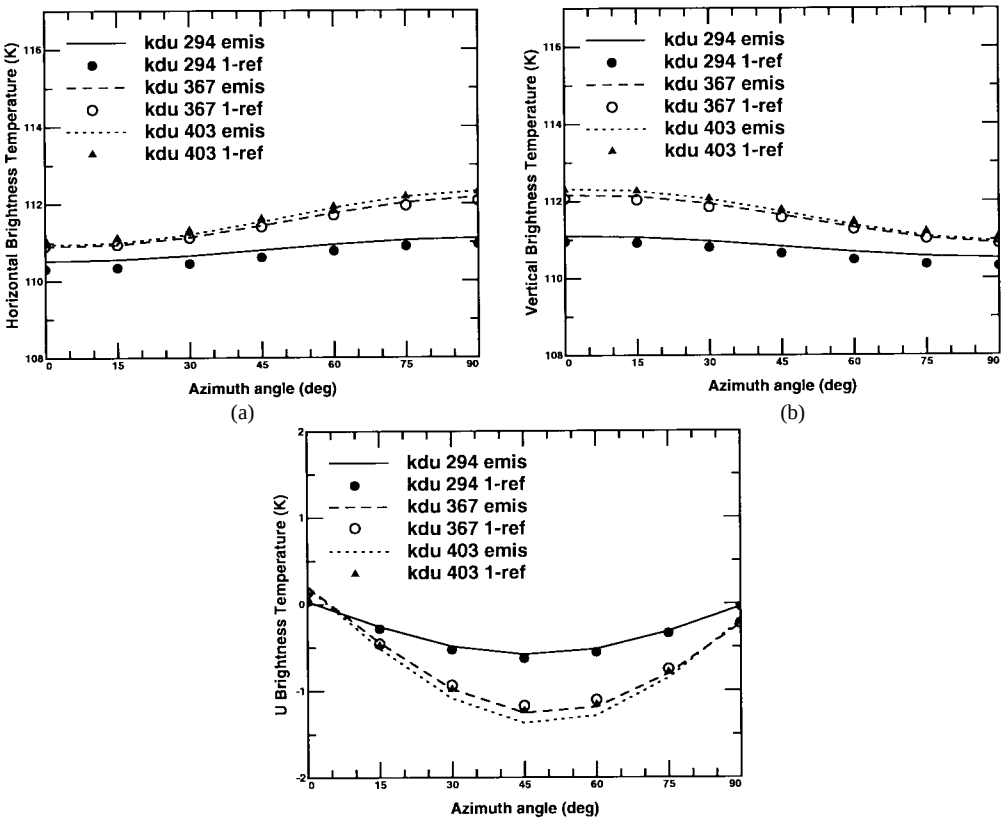

Fig. 1. Variation in SMFSIA/NIBC brightness temperatures with high-frequency ocean spectrum cutoff: 14-GHz, nadir looking, Durden–Vesecky spectrum, $U_{19.5} = 10$ m/s, surface temperature 283 K, $k_{dl} = 146.6$ rads/m: (a) T_{Bh}, (b) T_{Bv}, and (c) U_B.

spectral form of an arbitrary incident field gives

$$\overline{E}^{\text{inc}} = \int_{-\infty}^{\infty} dk_x \int_{-\infty}^{\infty} dk_y \, e^{i\overline{k}\cdot\overline{r}} \times \{E_{TM}(k_x, k_y)\hat{h}(-k_z) + E_{TE}(k_x, k_y)\hat{e}(-k_z)\} \tag{29}$$

$$\overline{H}^{\text{inc}} = \frac{1}{\eta_0} \int_{-\infty}^{\infty} dk_x \int_{-\infty}^{\infty} dk_y \, e^{i\overline{k}\cdot\overline{r}} \times \{E_{TM}(k_x, k_y)\hat{e}(-k_z) - E_{TE}(k_x, k_y)\hat{h}(-k_z)\} \tag{30}$$

where

$$\hat{h}(-k_z) = \hat{x}\,\frac{k_x k_z}{k k_\rho} + \hat{y}\,\frac{k_y k_z}{k k_\rho} + \hat{z}\,\frac{k_\rho}{k} \tag{31}$$

$$\hat{e}(-k_z) = \hat{x}\,\frac{k_y}{k_\rho} - \hat{y}\,\frac{k_x}{k_\rho}. \tag{32}$$

η_0 is the impedance of free space, $k_\rho = \sqrt{k_x^2 + k_y^2}$, $k_z = \sqrt{k^2 - k_\rho^2}$, $\overline{k} = \hat{x}k_x + \hat{y}k_y - \hat{z}k_z$, $k = \omega\sqrt{\mu_0 \epsilon_0}$, and $E_{\text{TE}}(k_x, k_y)$ and $E_{\text{TM}}(k_x, k_y)$ are the amplitudes of plane-wave spectral components with electric or magnetic fields polarized transverse to $\hat{z}$, respectively. Setting

$$E_{\text{TE}}(k_x, k_y) = \frac{g^2}{4\pi}\left(\frac{k k_x}{k_\rho k_z}\right) e^{-(k_x^2 g^2 + k_y^2 g^2)/4} \tag{33}$$

and

$$E_{\text{TM}}(k_x, k_y) = -\frac{g^2}{4\pi}\left(\frac{k_y}{k_\rho}\right) e^{-(k_x^2 g^2 + k_y^2 g^2)/4} \tag{34}$$

yields an incident field of

$$\overline{E}^{\text{inc}} = \frac{g^2}{4\pi} \int_{-\infty}^{\infty} dk_x \int_{-\infty}^{\infty} dk_y \, e^{i\overline{k}\cdot\overline{r}} \, e^{-(k_x^2 g^2 + k_y^2 g^2)/4} \times \left\{ \hat{x}\,\frac{k_x k_y}{k k_z} - \hat{y}\,\frac{k_z^2 + k_x^2}{k k_z} - \hat{z}\,\frac{k_y}{k} \right\} \tag{35}$$

$$\overline{H}^{\text{inc}} = \frac{g^2}{4\pi\eta_0} \int_{-\infty}^{\infty} dk_x \int_{-\infty}^{\infty} dk_y \, e^{i\overline{k}\cdot\overline{r}} \, e^{-(k_x^2 g^2 + k_y^2 g^2)/4} \times \left\{ -\hat{x} - \hat{z}\,\frac{k_x}{k_z} \right\} \tag{36}$$

where the zero $\hat{y}$ component of the magnetic field is evident along with the pure Gaussian form of the $\hat{x}$ component of the magnetic field

$$H_x^{\text{inc}} = -\frac{1}{\eta_0}\, e^{-(x^2 + y^2)/g^2} \tag{37}$$

since only a Gaussian function is involved in the Fourier transform. Such properties are useful when considering azimuthal variations in scattering at normal incidence since a clear polarization exists as opposed to other tapered beam choices

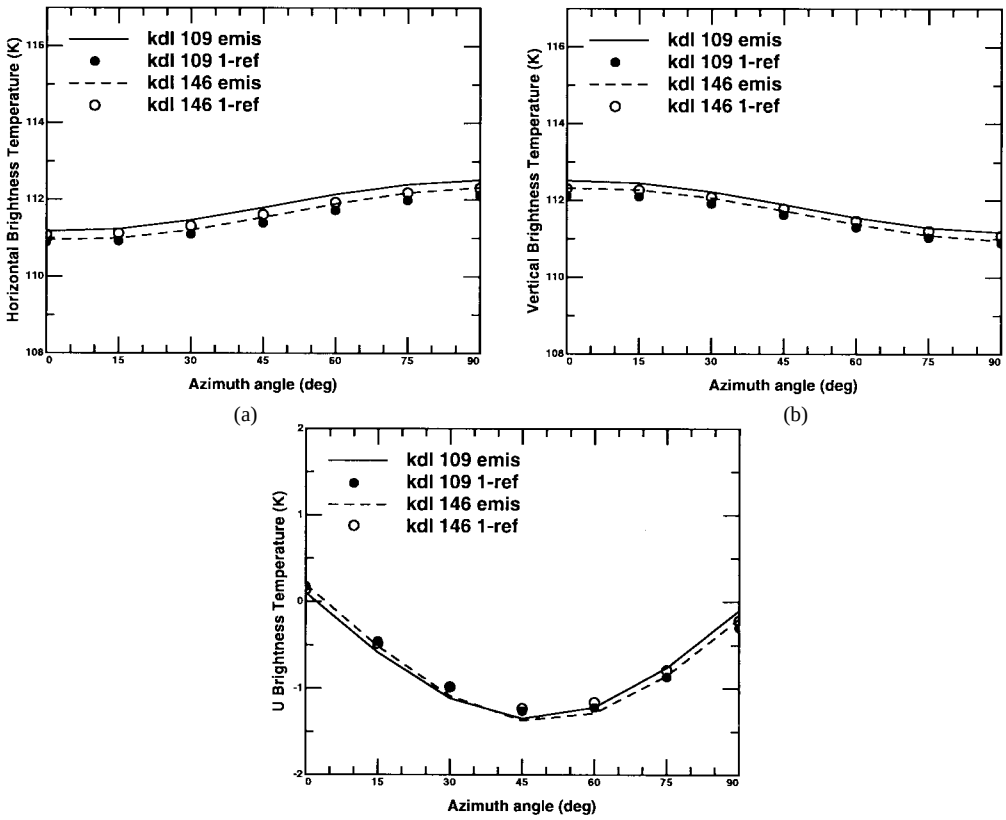

Fig. 2. Variation in SMFSIA/NIBC brightness temperatures with low-frequency ocean spectrum cutoff: 14-GHz, nadir looking, Durden–Vesecky spectrum, $U_{19.5} = 10$ m/s, surface temperature 283 K, $k_{du} = 403$ rads/m (a): T_{Bh}, (b) T_{Bv}, and (c) U_B.

for which there is no clear polarization at normal incidence [19]. Incident fields at other azimuthal angles were generated by rotating this field in azimuth. Note that this incident field has an azimuthally asymmetric plane-wave spectrum, which will eliminate the expected symmetries associated with nadir brightness temperatures. However, it will be shown in Section IX that these contributions are insignificant when compared with the azimuthal brightness temperature variations caused by the surface.

The above spatial expression for H_x^{inc} shows the parameter g of the incident field to be related to the width of the Gaussian beam, with larger values of g resulting in larger spots on the planar boundary. For the simulations of this paper, computational requirements limit surface sizes to $8\lambda \times 8\lambda$ or 64×64 points, so a $g = 1.5\lambda$ radius spot size on the surface was chosen to provide sufficient field attenuation at surface edges. This choice of g implies that ocean length scales larger than 3λ wavelength will not be resolved but will appear rather as "tilting" effects, so the simulations of Section IX will be include only surface length scales smaller than 3λ.

VI. SMFSIA Solution

The SMFSIA [18]–[22] is applied for the solution of matrix equation (25) once the appropriate submatrices are generated. The SMFSIA begins with the matrix equation rewritten as

$$\overline{\overline{Z}}\,\overline{F} = -\overline{F}^{\text{inc}}. \tag{38}$$

Nested iterative methods are applied for inversion of this matrix equation, given by

$$\left(\overline{\overline{Z}}^{(s)} + \overline{\overline{Z}}^{(\text{FS})}\right)\overline{F}^{(1)} = -\overline{F}^{\text{inc}} \tag{39}$$

$$\left(\overline{\overline{Z}}^{(s)} + \overline{\overline{Z}}^{(\text{FS})}\right)\overline{F}^{(n+1)} = -\overline{F}^{\text{inc}} - \overline{\overline{Z}}^{(w)}\overline{F}^{(n)} \tag{40}$$

where the original matrix $\overline{\overline{Z}}$ is decomposed into the sum of three matrices $\overline{\overline{Z}}^{(s)} + \overline{\overline{Z}}^{(FS)} + \overline{\overline{Z}}^{(w)}$ and (40) is iterated until convergence is observed in vector $\overline{F}$. Matrix $\overline{\overline{Z}}^{(s)}$, known as the "strong" matrix, contains the exact coupling between points within a certain radius of the testing point and zeros otherwise, making it a sparse matrix. Matrix $\overline{\overline{Z}}^{(FS)}$ contains an approximation to coupling between points far away from the surface, and it is known as the "flat surface" matrix because the approximation assumes that points lie at the same elevation. Matrix $\overline{\overline{Z}}^{(w)}$ corrects the approximation made in the flat surface matrix so that the sum of the three matrices is the original matrix equation of the MOM. Solution of the above matrix equations in the SMFSIA iterations is accomplished using an efficient conjugate gradient approach [32] in which required flat surface multiplies are performed with a fast Fourier transform. The above method remains an order N^2 technique since the weak matrix multiplies of each iteration are order N^2, but convergence is faster than a standard order N^2 conjugate gradient approach since weak matrix contributions are usually small; the method converged to within 0.1%

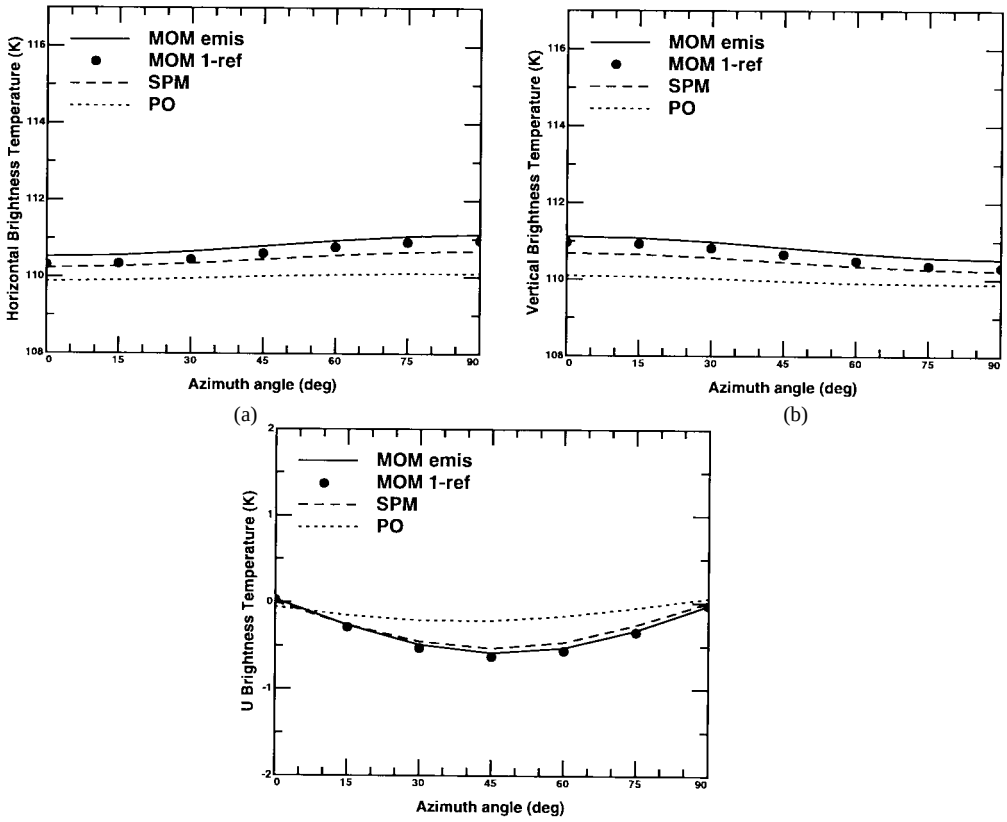

Fig. 3. Comparison of SMFSIA/NIBC and approximate theory brightness temperatures: 14-GHz, nadir looking, Durden–Vesecky spectrum, $U_{19.5} = 10$ m/s, surface temperature 283 K, $k_{dl} = 146.6$ rads/m, $k_{du} = 294$ rads/m: (a) T_{Bh}, (b) T_{Bv}, and (c) U_B.

accuracy in only a single iteration for the results illustrated in Section IX.

As discussed previously, weak and flat surface terms are neglected for the $\overline{\overline{R}}$ and $\overline{\overline{S}}$ matrices so that weak iterations are performed only on the free-space Green's function contributions. Since a conjugate gradient solver requires a product of the entire matrix of (25) with a vector, individual routines for submatrix products are used in succession and another conjugate gradient routine is used to obtain the $\overline{\overline{R}}^{-1}$ product by solving

$$\overline{\overline{R}}\begin{bmatrix}\overline{Q}_x\\ \overline{Q}_y\end{bmatrix} = \overline{\overline{S}}\begin{bmatrix}\overline{F}_x\\ \overline{F}_y\end{bmatrix} \tag{41}$$

where $\overline{Q}$ is the desired product with the matrix inverse and the right-hand side of the equation is known from earlier multiplications.

VII. Parallel Algorithm

Computational requirements for the SMFSIA/NIBC simulation are larger than those of [19] primarily due to the numerical integration and storage of lower medium matrix elements. The greater number of matrix vector products required at each conjugate gradient iteration and the conjugate iterations required for the calculation of $\overline{\overline{R}}^{-1}$ further increase the computational time needed. To reduce matrix element integration time so that calculations could be accomplished more efficiently, a parallel algorithm was developed and implemented using the IBM SP/2 400 node parallel computer at the Maui High Performance Computing Center [33]. The IBM SP/2 is a collection of 400 RS-6000 (based on a POWER2 CPU) workstations, capable of around 250 MFLOP operation individually, networked through a high-performance communication system to allow groups of nodes to operate in combination as a parallel processor. Software libraries are available at the center to implement interprocess communications using simple routine calls so that development of parallel codes is relatively efficient. The SMFSIA code of this paper uses the parallel virtual machine (PVM) message passing library [34], which is a public domain package for UNIX communications. The parallel algorithm developed is specifically for the simulations of this paper, in which polarimetric brightness temperatures at seven azimuth angles ranging from 0 to 90° will be presented.

Since brightness temperatures for a single surface realization can be calculated at varying observation angles by changing only the right-hand side (incident field) in (25), a group of seven SP/2 nodes was used with identical surface profiles and varying incident fields to obtain predictions at the seven azimuth angles desired. Since all seven nodes share the same matrix, integration of the $\overline{\overline{R}}$ and $\overline{\overline{S}}$ matrices is performed in parallel, with each node performing calculations for 1/7 of matrix rows and communicating the results to the other six processes to generate the full integrated matrices. Validation tests to be discussed in Section VIII also showed that an inte-

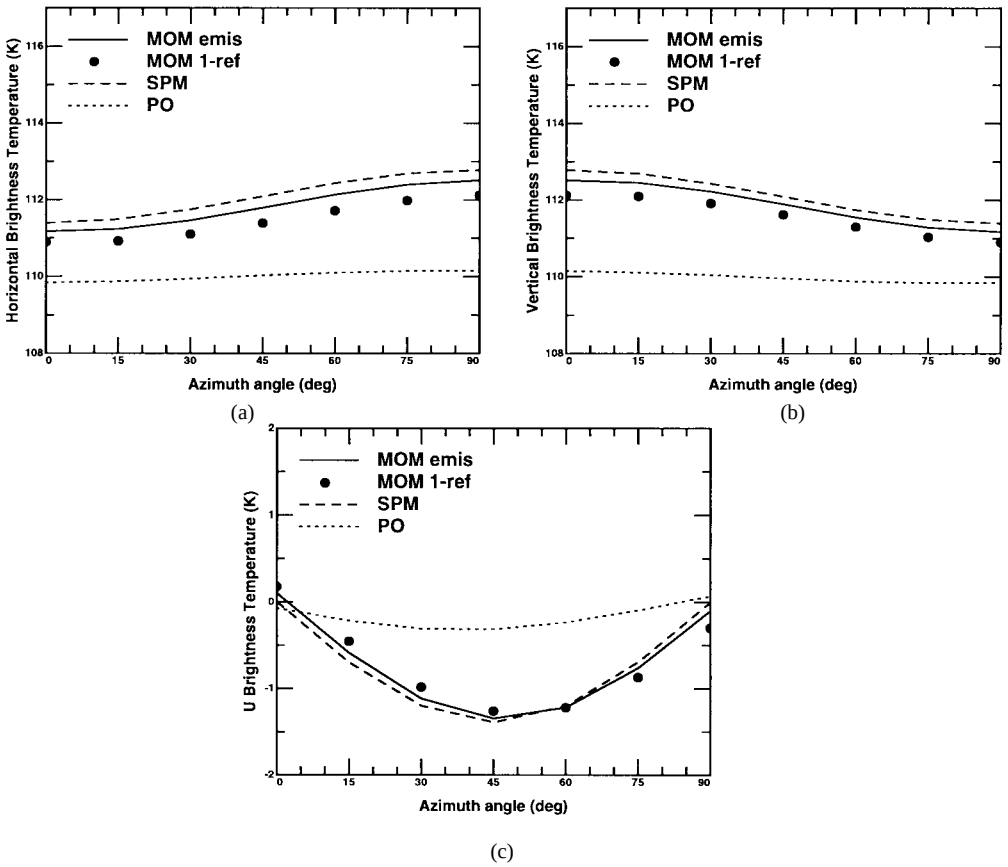

Fig. 4. Comparison of SMFSIA/NIBC and approximate theory brightness temperatures: 14-GHz, nadir looking, Durden–Vesecky spectrum, $U_{19.5} = 10$ m/s, surface temperature 283 K, $k_{dl} = 146.6$ rads/m, $k_{du} = 403$ rads/m: (a) T_{Bh}, (b) T_{Bv}, and (c) U_B.

gration of $\overline{\overline{T}}$ and $\overline{\overline{U}}$ matrix elements near the testing point was necessary for sufficient accuracy, so these integrations were also performed in parallel. Further parallelization was achieved by running multiple realizations in the Monte Carlo simulation simultaneously, with the final code using 64 nodes to compute seven azimuth angles for nine realizations simultaneously, with one node used for process control and monitoring. Results to be presented were averaged over nine realizations, for which comparisons of independent groups showed variations within 0.1 K.

VIII. Validation

A validation of the SMFSIA/NIBC method was performed by comparing numerical and analytical surface currents for a flat surface profile with the same permittivity $39.7 + i40.2$ to be used in Section IX. A closed form solution for the surface currents induced on a flat dielectric surface by the incident Gaussian beam of Section V was derived and is described in [35]. A direct comparison of the contribution of individual terms in the MOM integral equation revealed that integrations in the $\overline{\overline{R}}$, $\overline{\overline{S}}$, $\overline{\overline{T}}$, and $\overline{\overline{U}}$ matrices within the lower medium radius of two points were required to obtain agreement within 0.01 K of the flat surface result. Tests including lower medium matrix elements beyond the two point radius showed no influence on computed brightness temperatures, so this distance (equal to the 0.25 free-space wavelengths distance discussed in Section IV) was used in all further simulations. Brightness temperatures computed using $1 - r_a$ and e_a were in agreement to within 0.01 K when sampled at a rate of eight unknowns per free-space wavelength, indicating the high accuracy obtained by the numerical method for the flat surface case. It should be noted that absorbed and reflected powers in the SMFSIA/NIBC code are computed by integrating the normal component of the total and scattered Poynting vectors over the surface profile, respectively, rather than by integrating scattered far field powers over the upper hemisphere, which results in far less time required for brightness temperature calculation.

IX. Results

Fig. 1 illustrates SMFSIA/NIBC polarimetric brightness temperature predictions for the case studied in [10]: 14-GHz nadir observation of a Durden–Vesecky ocean surface (using $a_0 = 0.008$, as discussed in [10]) at a wind speed of $U_{19.5} = 10$ m/s. A lower cutoff wavenumber of $k_{dl} = 146.6$ rads/m (corresponding to an ocean length scale $L = 2\pi/k_{dl} = 2\lambda$, where λ is the 14-GHz electromagnetic wavelength in free space) for the ocean spectrum is used in the numerical simulation, and the high-frequency cutoff of the spectrum is changed to investigate the effects of the Bragg scatter portion of the spectrum on brightness azimuthal variations. The three plots of Fig. 1 show the T_{Bh}, T_{Bv}, and U_B brightnesses for azimuth angles ranging from 0 (upwind) to 90° (crosswind). V_B brightnesses are not plotted since all three models predict negligible V_B temperatures for nadir

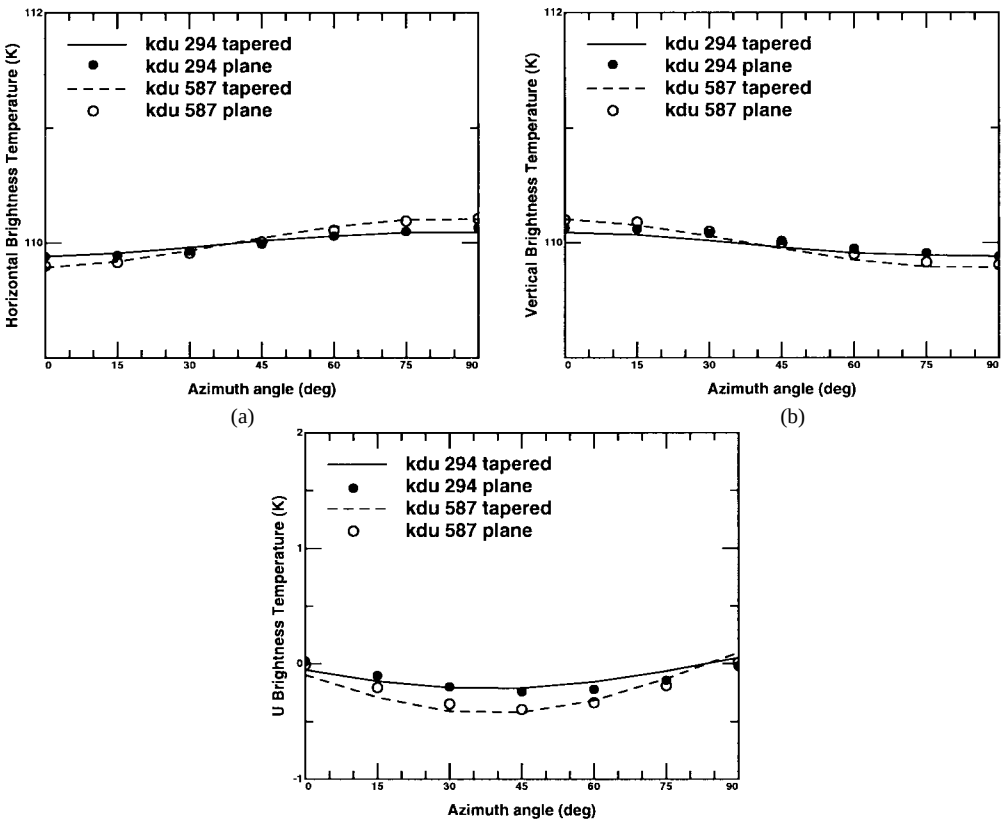

Fig. 5. Influence of tapered beam on PO brightness temperatures: 14-GHz, nadir looking, Durden–Vesecky spectrum, $U_{19.5} = 10$ m/s, surface temperature 283 K, $k_{dl} = 146.6$ rads/m: (a) T_{Bh}, (b) T_{Bv}, and (c) U_B.

observation. Brightness temperature calculations using the power absorbed into the lower medium and one minus the power reflected into the upper medium are illustrated by the lines and symbols, respectively, to indicate the level of error obtained from the numerical simulation. These errors are seen to be small compared to the overall level of azimuthal variations observed, especially in U_B brightnesses, indicating that sufficient accuracy is obtained for a meaningful result. The three curves in Fig. 1 clearly demonstrate the importance of the high-frequency portion of the ocean spectrum on nadir polarimetric brightness temperatures, at least for the Durden–Vesecky spectrum model considered. The small azimuthal variations observed for $k_{du} = 294$ rads/m are greatly increased as more high-frequency content is included, although a saturation effect is observed between the $k_{du} = 367$ rads/m and $k_{du} = 403$ rads/m cases. The electromagnetic wavenumber-surface rms height products ($k\sigma$) for these three cases were 0.137, 0.146, and 0.149, respectively.

Fig. 2 plots brightness temperatures for the configuration of Fig. 1 with low-frequency cutoffs of 146.6 rads/m ($k\sigma = 0.149$) and 109 rads/m ($k\sigma = 0.198$) and with a fixed high-frequency cutoff of 403 rads/m. Fig. 2 indicates that low-frequency components have little effect on nadir brightness temperatures with the Durden–Vesecky spectrum, as discussed in [10] and [11] with regard to the k_d parameter of these references. However, extensions beyond the $k_{dl} = 109$-rads/m limit (a surface wavelength of 2.7λ) were not possible due to increases in numerical power conservation error and beam resolution problems, so a full conclusion in this regard is not possible with the current numerical model.

SMFSIA/NIBC predictions are compared with those of the SPM (calculated following [10]) and PO (generated through Monte Carlo simulation) approximate models in Figs. 3 and 4. A low-frequency cutoff k_{dl} of 146.6 rads/m is used in both of these figures, with high-frequency cutoffs k_{du} of 294 and 403 rads/m used in Figs. 3 and 4, respectively, for $k\sigma$ products of 0.137 and 0.149. SMFSIA/NIBC results are observed to show similar trends to both SPM and PO predictions (all within 3 K of one another), although some important differences appear. PO predictions seemingly underestimate both the linear brightness temperatures and their azimuthal variations in both Figs. 3 and 4; the results are similar to those reported in [11], where SPM azimuthal variations were found to be underpredicted by a GO formulation, although a full ocean spectrum was considered in the reference. SPM results are seen to be in agreement in Fig. 3, where only a very small part of the ocean spectrum is simulated, but overpredict linear brightness temperatures in Fig. 4 when more high-frequency content is included. Brightness temperature azimuthal variations obtained from the SPM, however, are in agreement with numerical results in both cases.

Figs. 3(c) and 4(c) clearly illustrate the azimuthal asymmetry incurred by the tapered incident wave in the SMF-

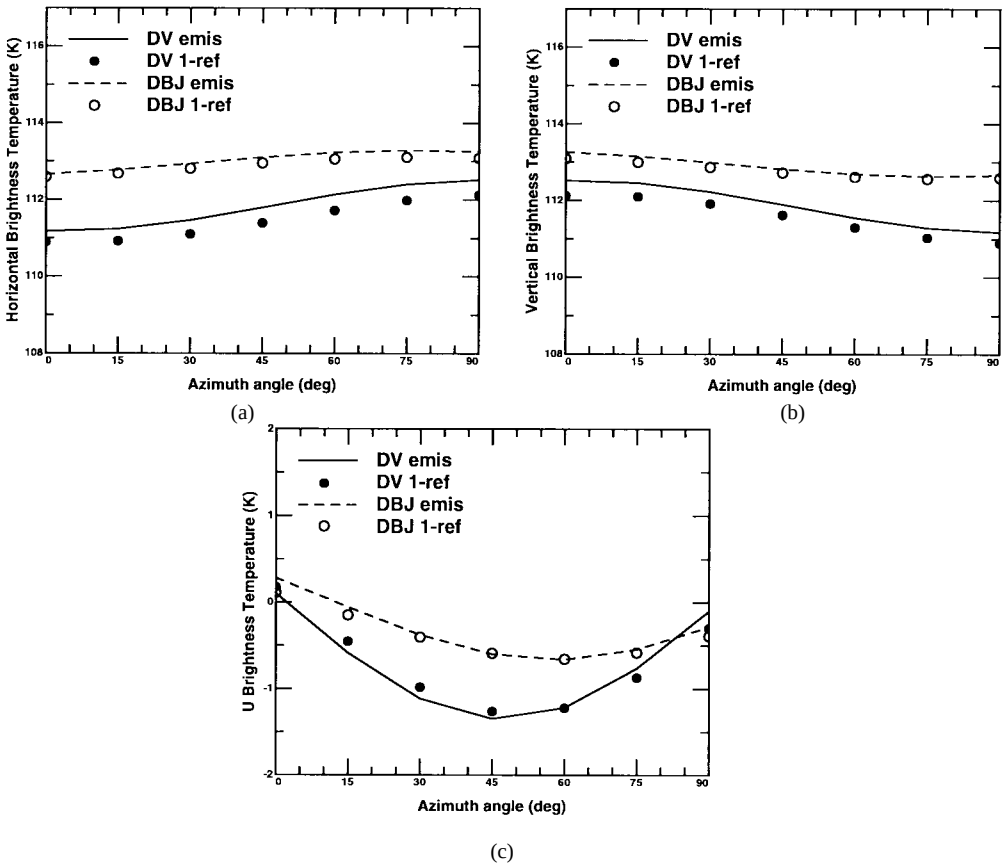

Fig. 6. Variation of SMFSIA/NIBC brightness temperatures with ocean spectral model: 14-GHz, nadir looking, $U_{19.5} = 10$ m/s, surface temperature 283 K, $k_{dl} = 109$ rads/m, $k_{du} = 403$ rads/m: (a) T_{Bh}, (b) T_{Bv}, and (c) U_B.

SIA/NIBC when compared to symmetric plane-wave SPM U_B predictions. The magnitude of this influence on polarimetric brightness temperatures in the simulation is assessed in Fig. 5, where PO brightness temperatures are compared for tapered beam and plane-wave incident fields. Use of the PO allows plane-wave incidence without edge diffraction effects since only a simple facet model PO formulation is used. Fig. 5 shows that although tapered beam fields cause azimuthal asymmetries in obtained brightness temperatures, the magnitude of azimuth variations observed is not significantly influenced by the tapered beam, so that SMFSIA/NIBC tapered beam results can be assumed to be representative of the corresponding plane-wave signatures.

Fig. 6 illustrates the influence of differing ocean spectrum models on SMFSIA/NIBC computed brightness temperatures. Brightness obtained with the Durden–Vesecky spectrum are compared with those of the Donelan–Banner–Jahne (DBJ) spectrum [36] for $k_{dl} = 109$ rads/m and $k_{du} = 403$ rads/m. The DBJ spectrum used is modified slightly from that of [36] in that the spectrum is made origin symmetric by reflecting the first quadrant over appropriate axes to generate all four quadrants of the spectrum. An appropriate scaling factor is used to maintain a constant surface rms height. This procedure was necessary to symmetrize the DBJ spectrum, while maintaining a maximum amplitude in the up–down wind direction due to the nonstationary properties of the original spectrum. The differing forms of the Durden–Vesecky and DBJ spectra in the capillary wave region lead to differing $k\sigma$ products of 0.198 and 0.224 for Durden–Vesecky and DBJ cases, respectively, and the two ocean models are also seen to lead to significantly different predictions of brightness temperatures. These comparisons are of interest because the Durden–Vesecky spectrum places the azimuthally anisotropic portion of the spectrum in the high-frequency region, so that lower frequencies are almost isotropic and therefore inherently do not contribute to brightness temperature azimuthal variations. In contrast, the DBJ spectrum of [36] places more azimuthal anisotropy into the lower frequency ocean waves, which can potentially lead to a different conclusion regarding the source of azimuthal variations obtained. These issues show that a better understanding of ocean wave azimuthal anisotropy is needed before realistic models of ocean polarimetric thermal emission can be developed.

X. Conclusions

An initial numerical study of ocean nadir polarimetric thermal emission has been performed using the SMFSIA/NIBC approach. The derivation of the NIBC method was presented, and variations in polarimetric brightness temperatures with spectral cutoffs were illustrated and found similar to those predicted by the analytical models. In particular, high-frequency components in the Durden–Vesecky ocean spectrum were found to be the principle sources of azimuthal variations in nadir ocean emission, as predicted by the SPM and PO meth-

ods. Comparisons with the approximate models showed the PO to significantly underpredict linear brightness temperatures and their azimuthal variations, while the SPM overpredicted linear brightness temperature levels but accurately predicted their azimuthal variations. A further comparison of brightnesses with the Durden–Vesecky and DBJ spectra showed these two spectra to yield differing predictions and the differing forms of the two spectra illustrate the limited current knowledge of ocean azimuthal dependencies. Thus, the development of future models for ocean polarimetric thermal emission will require a better understanding of the azimuthal properties of the ocean spectrum as well as the influence of other factors, such as atmospheric and surface foam emission and reflection of downwelling radiation into the radiometer field of view, none of which have been considered in this study.

REFERENCES

[1] L. Tsang, "Polarimetric passive microwave remote sensing of random discrete scatterers and rough surfaces," *J. Electromagn. Waves Applicat.*, vol. 5, pp. 41–57, 1991.

[2] M. E. Veysoglu, H. A. Yueh, R. T. Shin, and J. A. Kong, "Polarimetric passive remote sensing of periodic surfaces," *J. Electromagn. Waves Applicat.*, vol. 5, pp. 267–280, 1991.

[3] S. V. Nghiem, M. E. Veysoglu, J. A. Kong, R. T. Shin, K. O'Neill, and A. W. Lohanick, "Polarimetric passive remote sensing of a periodic soil surface: Microwave measurements and analysis," *J. Electromagn. Waves Applicat.*, vol. 5, pp. 997–1005, 1991.

[4] J. T. Johnson, J. A. Kong, R. T. Shin, D. H. Staelin, K. O'Neill, and A. Lohanick, "Third stokes parameter emission from a periodic water surface," *IEEE Trans. Geosci. Remote Sensing*, vol. 31, pp. 1066–1080, Nov. 1993.

[5] J. T. Johnson, J. A. Kong, R. T. Shin, S. H. Yueh, S. V. Nghiem, and R. Kwok, "Polarimetric thermal emission from rough ocean surfaces," *J. Electromagn. Waves Applicat.*, vol. 8, pp. 43–59, 1994.

[6] J. T. Johnson, R. T. Shin, and J. A. Kong, "Scattering and thermal emission from a two dimensional periodic surface," in *Progress in Electromagnetics Research 15*, J. A. Kong, Ed. Cambridge, MA: EMW, 1997, pp. 251–273.

[7] M. S. Dzura, V. S. Etkin, A. S. Khrupin, M. N. Pospelov, and M. D. Raev, "Radiometers polarimeters: Principles of design and applications for sea surface microwave emission polarimetry," in *Proc. IGARSS'92 Conf.*, pp. 1432–1434.

[8] Yu. A. Kratsov, A. V. Kuzmin, M. N. Pospelov, and A. I. Smirnov, "Surface wind measurements by radiometer-polarimeters in frame of Russia airspace programs," in *Proc. IGARSS'96 Conf.*, vol. 3, pp. 1454–1456.

[9] S. H. Yueh, S. V. Nghiem, W. Wilson, F. K. Li, J. T. Johnson, and J. A. Kong, "Polarimetric passive remote sensing of periodic water surfaces," *Radio Sci.*, vol. 29, pp. 87–96, 1994.

[10] S. H. Yueh, R. Kwok, F. K. Li, S. V. Nghiem, and W. J. Wilson, "Polarimetric passive remote sensing of ocean wind vectors," *Radio Sci.*, vol. 29, pp. 799–814, 1994.

[11] S. H. Yueh, S. V. Nghiem, and R. Kwok, "Comparison of a polarimetric scattering and emission model with ocean backscatter and brightness measurements," in *Proc. IGARSS'94 Conf.*

[12] S. H. Yueh, W. J. Wilson, F. K. Li, S. V. Nghiem, and W. B. Ricketts, "Polarimetric measurements of sea surface brightness temperatures using an aircraft K-band radiometer," *IEEE Trans. Geosci. Remote Sensing*, vol. 33, pp. 85–92, Jan. 1995.

[13] W. J. Wilson and S. H. Yueh, "JPL wind radiometer measurements," in *Proc. IGARSS'96 Conf.*, vol. 3, pp. 1447–1449.

[14] A. J. Gasiewski and D. B. Kunkee, "Polarized microwave emission from water waves," *Radio Sci.*, vol. 29, pp. 1449–1465, 1994.

[15] D. B. Kunkee and A. J. Gasiewski, "Airborne passive polarimetric measurements of sea surface anisotropy at 92 GHz," in *Proc. IGARSS'94 Conf.*

[16] ——, "Simulation of passive microwave wind direction signatures over the ocean using an asymmetric-wave geometrical optics model," *Radio Sci.*, vol. 32, p. 59, 1997.

[17] V. G. Irisov and Y. G. Trokhimovski, "Observation of the ocean brightness temperature anisotropy during the coastal ocean probing experiment," in *Proc. IGARSS'96 Conf.*, vol. 3, pp. 1457–1459.

[18] L. Tsang, C. H. Chan, and K. Pak, "Backscattering enhancement of a two dimensional random rough surface (three dimensional scattering) based on Monte Carlo simulations," *J. Opt. Soc. Amer.*, vol. 11, pp. 711–715, 1994.

[19] K. Pak, L. Tsang, C. H. Chan, and J. T. Johnson, "Backscattering enhancement of electromagnetic waves from two dimensional perfectly conducting random rough surfaces based on Monte Carlo simulations," *J. Opt. Soc. Amer.*, vol. 12, pp. 2491–2499, 1995.

[20] J. T. Johnson, L. Tsang, R. T. Shin, K. Pak, C. H. Chan, A. Ishimaru, and Y. Kuga, "Backscattering enhancement of electromagnetic waves from two dimensional perfectly conducting random rough surfaces: A comparison of Monte Carlo simulations with experimental data," *IEEE Trans. Antennas Propagat.*, vol. 44, pp. 748–756, June 1996.

[21] K. Pak, L. Tsang, and J. T. Johnson, "Numerical simulations and backscattering enhancement of electromagnetic waves from two dimensional dielectric random rough surfaces with sparse matrix canonical grid method," *J. Opt. Soc. Amer. A.*, vol. 14, pp. 1515–1529, 1997.

[22] J. T. Johnson, R. T. Shin, J. A. Kong, L. Tsang, and K. Pak, "A numerical study of the composite surface model for ocean scattering," *IEEE Trans. Geosci. Remote Sensing*, vol. 36, pp. 72–83, Jan. 1998.

[23] S. L. Durden and J. F. Vesecky, "A physical radar cross-section model for a wind driven sea with swell," *IEEE J. Oceanic Eng.*, vol. OE-10, pp. 445–451, Apr. 1985.

[24] F. J. Wentz, "Measurement of oceanic wind vector using satellite microwave radiometers," *IEEE Trans. Geosci. Remote Sensing*, vol. 30, pp. 960–972, July 1992.

[25] L. Tsang, J. A. Kong, and R. T. Shin, *Theory of Microwave Remote Sensing.* New York: Wiley, 1985.

[26] S. T. Wu and A. K. Fung, "A noncoherent model for microwave emissions and backscattering from the sea surface," *J. Geophys. Res.*, vol. 77, pp. 5917–5929, 1972.

[27] R. F. Harrington, "Matrix methods for field problems," *Proc. IEEE*, vol. 55, p. 136, Jan. 1967.

[28] J. J. H. Wang, *Generalized Moment Methods in Electromagnetics.* New York: Wiley, 1991.

[29] J. A. Kong, *Electromagnetic Wave Theory*, 2nd ed. New York: Wiley, 1990.

[30] L. A. Klein and C. T. Swift, "An improved model for the dielectric constant of sea water at microwave frequencies," *IEEE Trans. Antennas Propagat.*, vol. AP-25, pp. 104–111, 1977.

[31] K. M. Mitzner, "An integral equation approach to scattering from a body of finite conductivity," *Radio Sci.*, vol. 2, pp. 1459–1470, 1967.

[32] R. Barrett, M. Berry, T. Chan, J. Demmel, J. Donato, J. Dongarra, V. Eijkhout, R. Pozo, C. Romine, and H. van der Vorst, *Templates for the Solution of Linear Systems: Building Blocks for Iterative Methods*, available by ftp from ⟨netlib2.cs.utk.edu⟩, 1993.

[33] *Maui High Performance Computing Center World Wide Web Site*, on the World Wide Web at ⟨http:www.mhpcc.edu⟩, 1995.

[34] A. Geist, A. Beguelin, J. Dongarra, W. Jiang, R. Manchek, and V. Sunderam, "PVM 3 user's guide and reference manual," Oak Ridge Nat. Lab. Rep. ORNL/TM-12187, 1994.

[35] J. T. Johnson, "Surface currents induced on a dielectric halfspace by an incident Gaussian beam: An extended validation for point matching MOM codes," *Radio Sci.*, vol. 32, pp. 923–934, 1997.

[36] J. R. Apel, "An improved model of the ocean surface wave vector spectrum and its effects on radar backscatter," *J. Geophys. Res.*, vol. 99, pp. 16 269–16 291, 1994.

Joel T. Johnson (M'96) received the B.S. degree in electrical engineering from the Georgia Institute of Technology, Atlanta, in 1991 and the M.S. and Ph.D. degrees from the Massachusetts Institute of Technology, Cambridge, in 1993 and 1996, respectively.

He is currently an Assistant Professor in the Department of Electrical Engineering and ElectroScience Laboratory, The Ohio State University, Columbus. His research interests are in the areas of microwave remote sensing, propagation, and electromagnetic wave theory.

Dr. Johnson is a member of Tau Beta Pi, Eta Kappa Nu, and Phi Kappa Phi. He held a National Science Foundation Graduate Fellowship from 1991 to 1995, received the 1993 Best Paper Award from the IEEE Geoscience and Remote Sensing Society, and received the 1997 National Science Foundation CAREER, Office of Naval Research Young Investigator, and PECASE awards.

Robert T. Shin (S'82–M'83–SM'90) received the B.S., M.S., and Ph.D. degrees, all in electrical engineering from the Massachusetts Institute of Technology (MIT), Cambridge, in 1977, 1980, and 1984, respectively.

He has been with MIT's Lincoln Laboratory as a Research Staff Member from 1984 to 1989, as a Senior Staff Member from 1989 to 1992, and as an Assistant Group Leader since 1992. His research interests include electromagnetic wave scattering and propagation and theoretical model development and data interpretation for microwave remote sensing. He is a coauthor of *Theory of Microwave Remote Sensing* (New York: Wiley, 1985).

Dr. Shin is a member of The Electromagnetics Academy, American Geophysical Union, Tau Beta Pi, Eta Kappa Nu, and Commission F of the International Union of Radio Science. Since 1987, he has served on the editorial board of the *Journal of Electromagnetic Waves and Applications* (JEWA).

Jin Au Kong (S'65–M'69–SM'74–F'85) is a Professor of electrical engineering at the Massachusetts Institute of Technology (MIT), Cambridge. He has published eight books, including *Electromagnetic Wave Theory* (New York: Wiley, 1990), more than 400 refereed articles and book chapters, and supervised more than 120 theses. He is Editor-in-Chief of the *Journal of Electromagnetic Waves and Applications*, Chief Editor of the book series *Progress in Electromagnetics Research*, and Editor of the *Wiley Series in Remote Sensing*. His research interests include electromagnetic wave theory and applications.

Leung Tsang (S'73–M'75–SM'85–F'90) received the B.S, M.S, and Ph.D. degrees from the Massachusetts Institute of Technology (MIT), Cambridge, in 1971, 1973, and 1976, respectively.

He has been a Professor of electrical engineering at the University of Washington, Seattle, since 1986. He is coauthor of the book *Theory of Microwave Remote Sensing* (New York: Wiley, 1985). His current research interests include remote sensing, wave propagation in random media and rough surfaces, and optoelectronics.

Dr. Tsang is a Fellow of the Optical Society of America. He was the Technical Program Chairman of the 1994 IEEE Antennas and Propagation International Symposium and the Technical Program Chairman of the 1995 Progress in Electromagnetics Research Symposium in Seattle. Since 1996, he has been the Editor-in-Chief of the IEEE TRANSACTIONS ON GEOSCIENCE AND REMOTE SENSING.

Kyung Pak received the B.S., M.S.E.E., and Ph.D. degrees in 1990, 1992, and 1996, respectively, from the University of Washington. Seattle.

He has been with the Radar Science and Engineering Section, Jet Propulsion Laboratory, California Institute of Technology, Pasadena, since 1996. Currently, he is engaged in the studies of spaceborne scatterometer processing. His research interests include electromagnetic wave scattering from irregular and random rough surfaces, numerical simulation of wave scattering, and scatterometer processing.